

1 Hydrometeor Storage and Advection Effects in DYNAMO Budget Analyses

2 Richard H. Johnson, Paul E. Ciesielski, and Wayne H. Schubert

3 *Department of Atmospheric Science, 1371 Campus Delivery, Colorado State University, Fort*
4 *Collins, CO 80523*

5 *Corresponding author:* Richard H. Johnson, Richard.H.Johnson@colostate.edu

6 ABSTRACT: The Dynamics of the Madden-Julian Oscillation (MJO) field campaign (DYNAMO)
7 over the central Indian Ocean captured three strong MJO events during October-December 2011.
8 Using the conventional budget approach of Yanai et al., surface rainfall P_0 is computed as a residual
9 from the vertically integrated form of the moisture budget equation. This budget-derived P_0 is
10 spatially averaged over the Gan Island NCAR S-PolKa radar domain and compared with rainfall
11 estimates from the radar itself. To isolate the MJO signal, these rainfall time series are low-pass
12 (LP) filtered and a three-MJO composite is created based on the time of maximum LP-filtered
13 S-PolKa rainfall for each event. A comparison of the two composite rainfall estimates shows
14 that the budget rainfall overestimates the radar rainfall by $\sim 15\%$ in the MJO build-up stage and
15 underestimates radar rainfall by $\sim 8\%$ in the MJO decay stage. These rainfall differences suggest
16 that hydrometeor (clouds and rain) storage and advection effects, which are neglected in the budget
17 approach, are likely significant. Satellite and ground-based observations are used to investigate
18 these hydrometeor storage and advection effects. While the findings are qualitatively consistent
19 with expectations from theory, they fall short of explaining their full magnitude, suggesting even
20 more refined experimental designs and measurements will be needed to adequately address this
21 issue.

22 **1. Introduction**

23 The methodology to diagnose the properties of tropical cloud clusters introduced by Yanai
24 et al. (1973) has been utilized in numerous studies. This procedure has been valuable in many
25 applications, yet continued advances in measurement technology motivate the use of a more
26 accurate treatment of thermodynamics in such budget analyses. In the Yanai et al. diagnostic
27 framework, referred to here as the conventional budget method or CBM, moist static energy is
28 assumed to be conserved, apart from radiative effects. It is also assumed that the latent heat
29 of condensation L is constant, such that important physical effects of ice (freezing, melting,
30 deposition, sublimation) are neglected. In addition, the storage and advection of cloud condensate
31 and precipitating hydrometeors are not considered. Under certain conditions these effects can be
32 important (Peixoto and Oort 1992).

33 These complicating factors associated with the conventional budget approach can be interpreted
34 physically in the following way as they relate to MJO convection. First, with respect to storage,
35 as the cloud field increases during the developing phase of the MJO, cloud condensate is “stored”
36 in the atmosphere rather than precipitating out immediately. The reverse effect holds true during
37 the decaying phase. Secondly, advection in deep convective systems can transport hydrometeors
38 into or out of a sampling volume, which can also contribute to errors in traditional budgets that
39 exclude these effects. Johnson (1980) estimated that the neglect of cloud storage effects resulted
40 in errors on the order of 20% in the column integrated moisture budget during periods of rapidly
41 evolving cloud fields in Atlantic tropical easterly waves. On even shorter time scales, cloud
42 storage and hydrometeor advection effects are particularly important, such as in the case of diurnal
43 thunderstorm development (McNab and Betts 1978) and squall line evolution (Gallus and Johnson
44 1991).

45 Ooyama (1990, 2001) proposed a very accurate form of moist thermodynamics for use in tropical
46 models, namely, one that includes hydrometeor storage and advective effects. His formulation
47 of moist thermodynamics is not limited to modeling studies but can also be used in heat and
48 moisture budget studies (Schubert et al. 2018). With the advent of radiosondes with GPS-derived
49 winds and the recent availability of certain satellite data products, this more accurate treatment of
50 moist thermodynamics provides the opportunity to refine diagnostic analyses of a wide range of
51 precipitation systems. As a preliminary effort toward this end, hydrometeor storage and advective

52 effects in thermodynamic budgets are evaluated using observations from the 2011-12 Dynamics
53 of the MJO (DYNAMO) field campaign. The strategy is to compare CBM-diagnosed rainfall
54 rate estimates with independent estimates of those quantities obtained from ground and space-
55 based remote sensing platforms. While the lack of precise measurements of hydrometeor storage
56 and advection in DYNAMO precipitation systems limits the extent to which these processes
57 can be accurately evaluated, these comparisons yield insight into their aggregate impacts on the
58 thermodynamic budgets.

59 **2. Data and Methods**

60 *a. Data*

61 Observations used in this study are from the DYNAMO field campaign, conducted from October
62 2011 through March 2012 over the central Indian Ocean (Yoneyama et al. 2013). DYNAMO was
63 designed to investigate processes associated with the initiation of the Madden-Julian Oscillation
64 or MJO (Madden and Julian 1971). The sounding network established during DYNAMO was
65 comprised of two quadrilateral arrays straddling the equator. This network forms the basis of our
66 study, with a focus on the period 2 October through 31 December when the overall network was
67 most complete and 4-8 sounding launches per day were achieved (Ciesielski et al. 2014). Three
68 prominent MJOs occurred in the DYNAMO domain during this 3-month period (Gottschalck et al.
69 2013). The Atmospheric Radiation Measurement Program (ARM) operated a supersite located
70 at Gan island (0.69° S, 73.2° E) as part of the ARM MJO Investigation Experiment (AMIE). This
71 site had multiple radars and radiometers, as well as 8-per-day sounding observations. In addition,
72 the National Center for Atmospheric Research S-band dual polarization Doppler radar S-PolKa
73 (SPOL) was deployed on Gan Island. SPOL provides rainfall rate estimates that can be compared
74 to those determined from atmospheric sounding budgets. The sounding and radar datasets were
75 quality-controlled and bias corrected in connection with a special effort to create a DYNAMO
76 legacy dataset (Ciesielski et al. 2014; Xu et al. 2015).

77 Other data used in this study include cloud liquid and ice paths as well as fractional cloud amount
78 from the Clouds and the Earth's Radiant Energy System (CERES) product at 3-h resolution on a 1°
79 grid (Wielicki et al. 1996). Also used are liquid and ice water path (LWP and IWP) estimates from
80 the Pacific Northwest National Laboratory (PNNL) Combined Retrieval (CombRet) product based

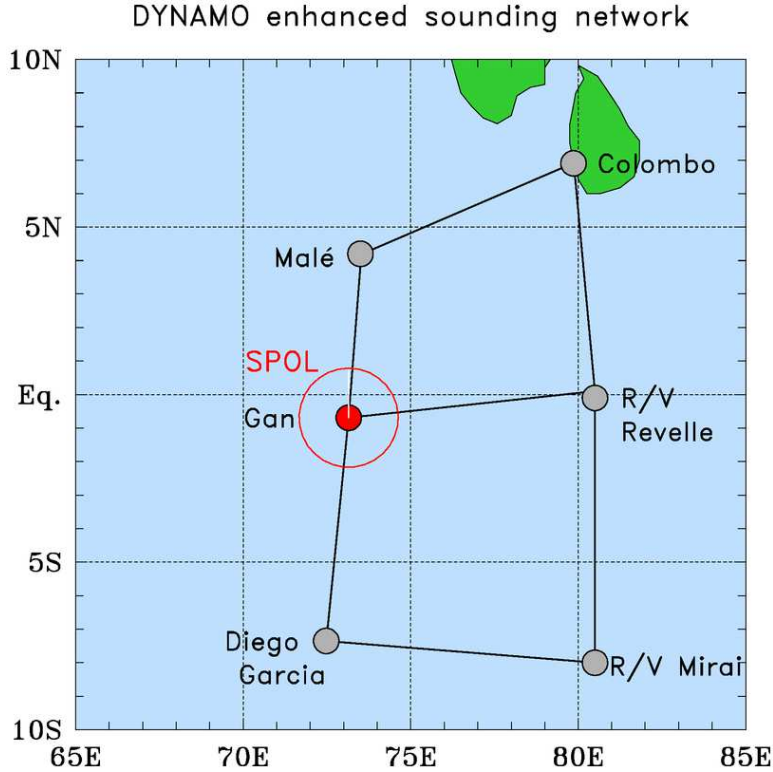
on cloud profiles, provided primarily by a zenith-pointing Doppler Ka-band cloud radar (KAZR) merged with SPOL observations, and incorporating sounding-based thermodynamic measurements at Gan Island (Feng et al. 2014). This combined product provides estimates of LWP and IWP, as well as liquid water content (LWC) and ice water content (IWC), although values of IWC in cirrus are underestimated at times due to attenuation by heavy precipitation (Shell et al. 2020). The 30-s product used in this study was averaged into 3-h bins and is available for the period from 10 October 2011 to 08 February 2012. The TropFlux product (Praveen Kumar et al. 2012) provided estimates of surface sensible and latent heat fluxes at daily resolution on a 1° grid. European Center for Medium-Range Weather Forecasts (ECMWF) operational analysis (OA) used in this study was available at 0.25 degree horizontal resolution, 20 vertical levels from the surface to 20 hPa, and 6-h intervals. Though not directly used in the analyses in this paper, rainfall estimates from the Tropical Rainfall Measuring Mission (TRMM) 3B42v7 product are shown simply for the purposes of comparison to the other rainfall estimates. This TRMM rainfall product is at 0.25, 3 h resolution (Huffman et al. 2007).

A composite of the three MJOs during DYNAMO was created by applying a low-pass (LP) Kaiser filter (Hamming 1989) in time to retain variability at frequencies twenty days and longer. The composite is constructed in terms of days before and after the time of maximum LP-filtered SPOL rainfall (Lag 0). With the application of this filter, six days of 3-h data are lost at the ends of the filtered time series (Ciesielski et al. 2017).

100 b. Conventional budget method (CBM)

101 In constructing the CBM gridded analyses for this study, ECMWF OA data were used at 5° grid intersections if no observations (soundings, satellite winds, or otherwise) were present within a 102 4.5° radius of such an intersection. This procedure was used to enhance data coverage outside the 103 main sounding arrays, so results in the interior are largely independent of model analyses and hence 104 parameterizations of physical processes (Johnson et al. 2015). Following interpolation of the OA 105 data to 3-hourly intervals, the sounding data, along with the other observations and model fields 106 described above, were objectively analyzed onto a 1° grid at the surface and at 25-hPa intervals 107 from 1000 to 50 hPa over the entire domain shown in Fig. 1 using the multiquadric interpolation 108 procedure as described in Ciesielski et al. (1997). CBM rainfall estimates that are compared to 109

110 SPOL measurements are based on averages of the grid points that fall within the 150-km radius of
 111 the SPOL surveillance area.



112 Fig. 1. Map showing the DYNAMO enhanced sounding network. Observations for this study are focused on
 113 the Gan Island site (red dot) at 0.69°S, 73.15°E. Outer red circle around Gan indicates the 150-km range ring for
 114 the SPOL radar. Budget-estimated rainfall was averaged over this area for comparison to SPOL estimates.

115 The apparent heat source Q_1 and apparent moisture sink Q_2 are computed using the following
 116 heat and moisture budget equations of Yanai et al. (1973) written with z as the vertical coordinate:

$$Q_1 \equiv \frac{\partial \bar{s}}{\partial t} + \bar{\mathbf{v}} \cdot \nabla \bar{s} + \bar{w} \frac{\partial \bar{s}}{\partial z} = -\frac{\partial (\bar{\rho}_a \bar{w}' s')}{\bar{\rho}_a \partial z} + L(\bar{c} - \bar{e}) + \bar{Q}_R \quad (1)$$

$$Q_2 \equiv -L \left(\frac{\partial \bar{q}_v}{\partial t} + \bar{\mathbf{v}} \cdot \nabla \bar{q}_v + \bar{w} \frac{\partial \bar{q}_v}{\partial z} \right) = -L \frac{\partial (\bar{\rho}_a \bar{w}' q'_v)}{\bar{\rho}_a \partial z} + L(\bar{c} - \bar{e}) \quad (2)$$

117 where $s = c_p T + gz$ is the dry static energy, q_v is the water vapor mixing ratio, ρ_a is the density of
 118 dry air, L is the latent heat of condensation, c is the condensation rate, e the evaporation rate, Q_R
 119 is the radiative heating rate, and overbar refers to a horizontal average. The averaging area for this

120 study is the 150-km range ring around the SPOL radar as shown in Fig. 1. Vertically integrating
 121 (1) and (2) from the surface to the tropopause yields the following integral constraints:

$$\langle Q_1 \rangle = LP_0 + \langle Q_R \rangle + S_0, \quad (3)$$

$$\langle Q_2 \rangle = L(P_0 - E_0), \quad (4)$$

122 where $\langle \cdot \rangle = \int_0^{z_T} (\cdot) \bar{\rho}_a dz$, z_T is the height of the tropopause, and $S_0 = (\bar{\rho}_a c_p \bar{w'} \bar{T'})_0$ and $LE_0 =$
 123 $(L\bar{\rho}_a \bar{w'} \bar{q'_v})_0$ are the surface sensible and latent heat fluxes, respectively.

124 Combining (3) and (4) yields

$$\langle Q_1 \rangle - \langle Q_2 \rangle - \langle Q_R \rangle = S_0 + LE_0, \quad (5)$$

125 Using surface measurements of S_0 and E_0 , surface precipitation P_0 can be computed from (4) and
 126 column net radiative heating rate $\langle Q_R \rangle$ from (5) and then compared to independent measurements
 127 of those quantities in order to determine the reliability of the budgets. However, as discussed in
 128 Yanai and Johnson (1993), Ooyama (2001), and Schubert et al. (2018), equations (1) and (2)
 129 are only approximations in that they omit storage and advection of hydrometeors, effects of ice
 130 processes, and contributions to entropy changes from dry air, water vapor, cloud condensate, and
 131 precipitation.

132 *c. More accurate budget equations*

133 To begin with, consider the conventional budget equation (4) rewritten in the form

$$P_0 = E_0 + \frac{\langle Q_2 \rangle}{L} = E_0 - \int_0^{z_T} \left(\frac{\partial \bar{q}_v}{\partial t} + \bar{\mathbf{v}} \cdot \nabla \bar{q}_v + \bar{w} \frac{\partial \bar{q}_v}{\partial z} \right) \bar{\rho}_a dz. \quad (6)$$

134 This equation is well suited for use with data from a network of radiosonde stations since with
 135 an independent estimate of E_0 , sounding data provide all fields needed to compute P_0 . However,
 136 the more accurate form of (6) includes the effects of cloud condensate and falling precipitation
 137 (Ooyama 2001; Schubert et al. 2018):

$$P_A = E_0 + \frac{<Q_2>_A}{L} = E_0 - \int_0^{z_T} \left(\frac{\partial \bar{q}_T}{\partial t} + \bar{\mathbf{v}} \cdot \nabla \bar{q}_T + \bar{w} \frac{\partial \bar{q}_T}{\partial z} \right) \bar{\rho}_a dz , \quad (7)$$

138 where $q_T = q_v + q_c + q_r$, q_c is the airborne condensed water (including both liquid q_l and ice q_i), q_r
139 is the precipitating water, and subscript A refers to the more accurate quantities. E_0 is given by the
140 expression in Section 2.b as long as there is no cloud condensate (fog) at the ground. Subtracting
141 (6) from (7) yields an expression for a more accurate estimate (P_A) of the precipitation rate:

$$P_A = P_0 - \int_0^{z_T} \left(\frac{\partial \bar{q}_H}{\partial t} + \bar{\mathbf{v}} \cdot \nabla \bar{q}_H + \bar{w} \frac{\partial \bar{q}_H}{\partial z} \right) \bar{\rho}_a dz , \quad (8)$$

142 where $q_H \equiv q_c + q_r$ is the hydrometeor contribution to q_T . This equation states that the computed
143 precipitation P_0 may differ from P_A due to local changes in q_H (referred to here as storage
144 effects) and secondly by advective effects given by the latter two terms in parentheses on the
145 RHS of (8). Concerning storage, when the hydrometer field is increasing, i.e., $\partial q_H / \partial t > 0$,
146 P_0 will overestimate P_A , while the opposite effect is true when the hydrometer field is decreasing
147 ($\partial q_H / \partial t < 0$). Physically, this means that when cloud and precipitation area coverage is increasing,
148 rather than falling out or evaporating, hydrometeors are “stored” in the growing population of clouds
149 and precipitation. Hydrometeor storage can be important on time scales ranging from individual
150 convective systems (Gallus and Johnson 1991) up to, as will be shown here, the time scale of the
151 MJO.

152 The other complicating factor relates to hydrometeor transport. For example, hydrometeors
153 generated in an averaging volume during a certain time period may be transported out of the
154 volume, precipitating or evaporating elsewhere. Using the expression for the conservation of mass,
155 (8) can be written in flux form:

$$P_A = P_0 - \int_0^{z_T} \left(\frac{\partial \bar{\rho}_a \bar{q}_H}{\partial t} + \nabla \cdot \bar{\rho}_a \bar{q}_H \bar{\mathbf{v}} + \frac{\partial}{\partial z} \bar{\rho}_a \bar{q}_H \bar{w} \right) dz . \quad (9)$$

156 Assuming $\bar{w} = 0$ at the surface and tropopause, (9) becomes

$$P_A = P_0 - \int_0^{z_T} \left(\frac{\partial \bar{\rho}_a \bar{q}_H}{\partial t} + \nabla \cdot \bar{\rho}_a \bar{q}_H \bar{\mathbf{v}} \right) dz . \quad (10)$$

157 The first term in parentheses in (10) once again refers to hydrometeor storage, while the second term
 158 represents hydrometeor transport into or out of the averaging volume. A column-net divergence
 159 of hydrometeors has the same effect as increasing hydrometeor storage, namely, it causes P_0 to
 160 overestimate P_A . This could occur, for example, at times of deep convection when there is a
 161 divergence of ice in the storm-top outflow layer. An investigation of the radial outflow of ice in
 162 the tropical tropopause transition layer atop mesoscale convective systems has been carried out by
 163 Virts and Houze (2015).

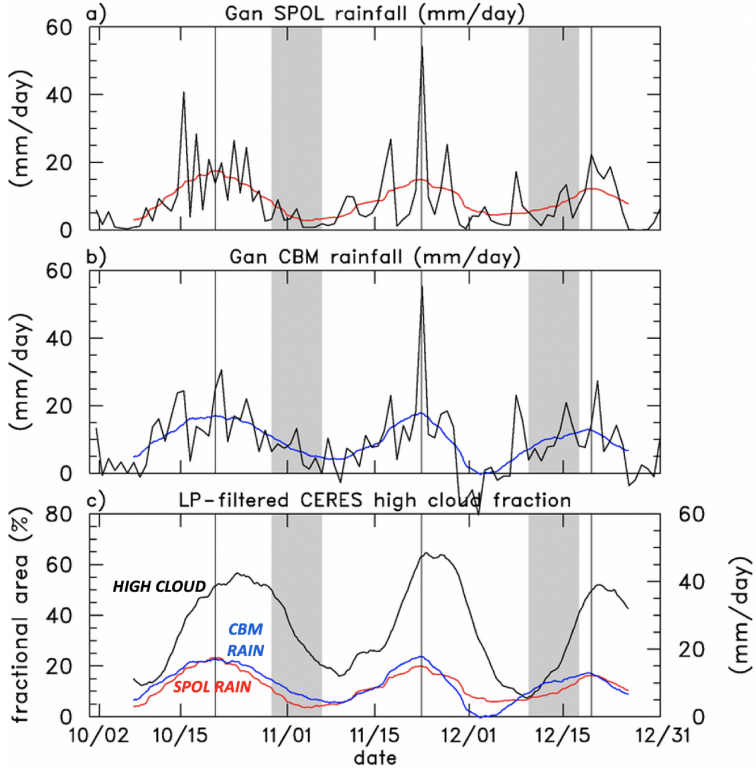
164 Similarly, a more accurate estimate of the column net radiative heating rate $\langle Q_R \rangle_A$ can be
 165 obtained from (5), (7), and (10):

$$\begin{aligned} \langle Q_R \rangle_A &= \langle Q_1 \rangle - \langle Q_2 \rangle_A - S_0 - LE_0 \\ &= \langle Q_1 \rangle - LP_A - S_0 \\ &= \langle Q_R \rangle + L \int_0^{z_T} \left(\frac{\partial \bar{\rho}_a \bar{q}_H}{\partial t} + \nabla \cdot \bar{\rho}_a \bar{q}_H \bar{\mathbf{v}} \right) dz . \end{aligned} \quad (11)$$

166 This result implies that storage of hydrometeors or the divergence of hydrometeors (say, in the
 167 convective outflow layer aloft) will lead to an underestimate of the actual column net radiative
 168 heating rate (excessive radiative cooling) based on the conventional budget method. While the
 169 effects of storage and advection of hydrometeors on budget estimates of radiative heating should,
 170 in principle, be discernible, the determination of Q_R as a residual from budgets is a rather sensitive
 171 calculation (Johnson and Ciesielski 2000; Johnson et al. 2015) and we have been unable to draw
 172 meaningful conclusions from attempts at such an analysis.

173 3. Results

179 Three-month long time series of daily-averaged and LP-filtered rainfall rates based on SPOL and
 180 the CBM Q_2 budget are shown in Figs. 2a and b. Thin vertical lines in the figure denote the times of
 181 the LP-filtered SPOL rainfall peaks associated with the October, November, and December MJOs.
 182 Notable features of the SPOL time series are (1) the prevalence of 2-day peaks that dominate the
 183 October MJO rainfall pattern (Zuluaga and Houze 2013; Yu et al. 2018), (2) several large rainfall
 184 peaks at \sim 5-day intervals during the November MJO associated with the passage of Kelvin waves

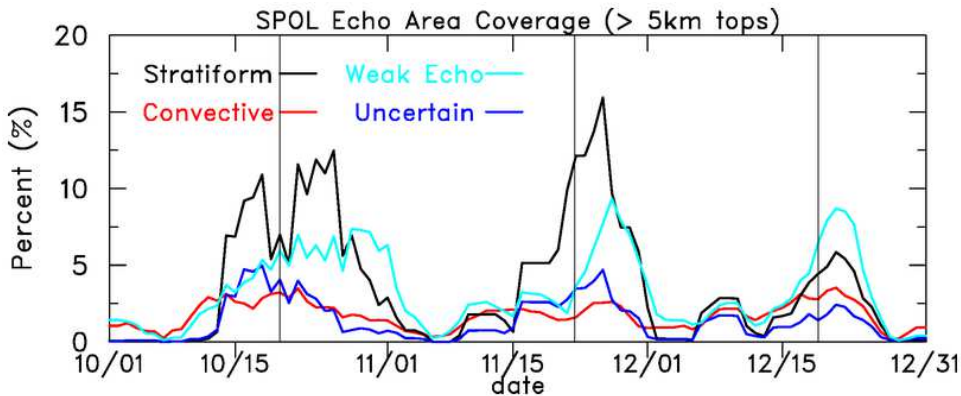


174 FIG. 2. Time series of (a) daily-averaged (black) and LP-filtered (red) SPOL rainfall rate, (b) daily-averaged
 175 (black) and LP-filtered (blue) budget-estimated rainfall averaged over SPOL radar domain shown in Fig. 1, and
 176 (c) CERES LP-filtered high-cloud fraction along with LP-filtered rainfall curves based on SPOL measurements
 177 (red) and the conventional budget method (CBM, blue). LP-filtered rainfall peaks for each MJO are indicated by
 178 thin vertical lines and time periods when R/V *Revelle* was off station by shading.

185 (Moum et al. 2014), and (3) the somewhat weaker amplitude of the December MJO. A comparison
 186 of the two LP-filtered rainfall time series is shown in Fig. 2c along with the CERES estimate
 187 of high-cloud fraction (HCF) over the SPOL radar domain, used as a proxy for the presence of
 188 hydrometers. One to two weeks prior to the peak rainfall for all three MJOs, the CBM rainfall
 189 rate exceeds the SPOL rate, while the reverse is true for the decay phases of the November and
 190 December MJOs. The different behavior during the decay phase of the October MJO could in part
 191 be related to the fact that the R/V *Revelle* was off station during a portion of this period (shading,
 192 Fig. 2), causing CBM results to be less reliable.

193 Another contributing factor, however, in explaining why CBM rain exceeded SPOL rain during
 194 late October is the complex evolution of convection that occurred during this period. Figure 3

195 shows a times series of the area coverage of various precipitation types using the classification
 196 methodology described in Powell et al. (2016) for SPOL echoes with tops above 5 km.¹ During late
 197 October, the area covered by stratiform precipitation experienced an overall increase followed by
 198 rapid a dropoff in the last week of the month. This evolution suggests that a storage of hydrometeors,
 199 perhaps aided by a concurrent increase in weak echoes (Fig. 3), could explain at least part of the
 200 positive CBM-SPOL difference in late October.

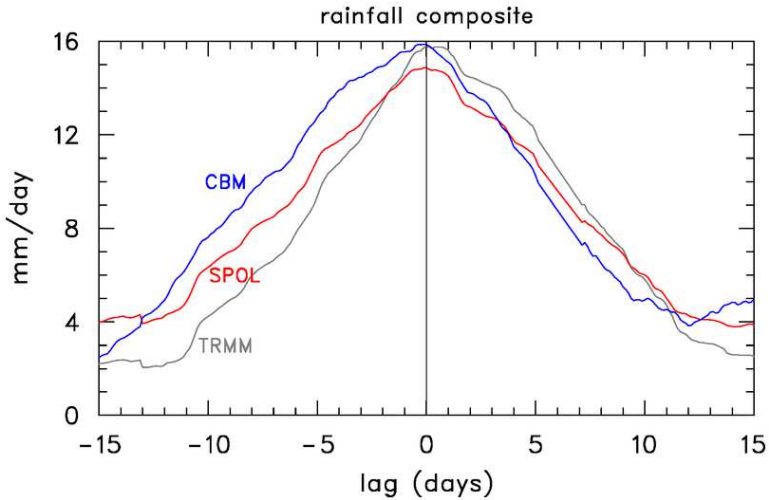


201 FIG. 3. Time series of 5-day running mean filtered echo area coverage precipitation categories (with echo tops
 202 exceeding 5 km) based on the classification scheme of Powell et al. (2016). Vertical lines indicate times of peak
 203 LP-filtered rainfall.

204 As is evident from Fig. 2b, there is considerable uncertainty in computed daily-averaged rainfall
 205 (even negative rain at times), largely due to sampling errors associated with sounding array budgets
 206 (Mapes et al. 2003). To reduce such errors, averaging in time is required, which is accomplished
 207 here by compositing the LP-filtered SPOL and CBM rainfall estimates for the three MJOs as
 208 shown in Fig. 4. TRMM rainfall rate estimates have been included for comparison. CBM rainfall
 209 rate estimates exceed SPOL estimates by $1-2 \text{ mm day}^{-1}$ leading up to the rainfall peak with the
 210 reverse being true post-peak, albeit to a lesser extent. This result is consistent with (8), which
 211 indicates that budgets should overestimate rainfall rates when the hydrometeor field is increasing
 212 and underestimate rainfall rates when the hydrometeor field is decreasing. The TRMM rainfall
 213 rates underestimate the SPOL values as convection builds up owing to TRMM undersampling
 214 small-scale convection, while TRMM overestimates the rainfall rates in the post-peak stage due to
 215 widespread cirrus anvils influencing TRMM estimates (Xu and Rutledge 2014). These deficiencies

¹In their procedure, weak precipitation features that have little implication for latent heating are described at Weak Echoes and those that surround convective cores that could not be classified as either convective or stratiform are referred to as Uncertain.

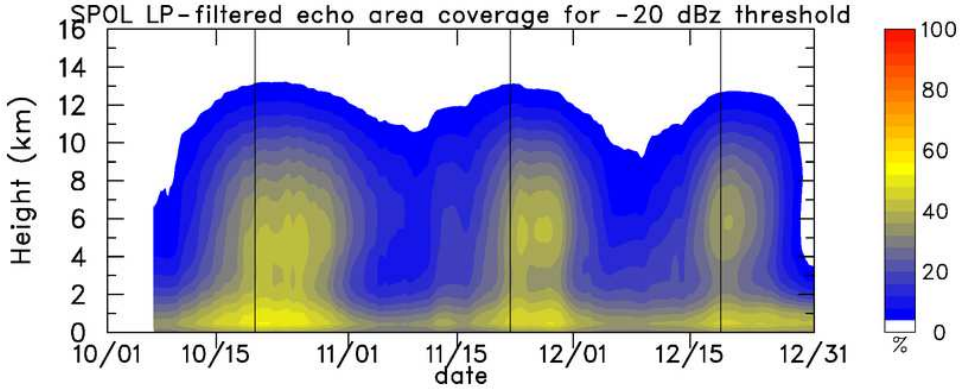
216 in the TRMM estimates preclude their use in the rather sensitive analyses of storage and advective
217 effects in thermodynamic budgets.



218 FIG. 4. Three-MJO composite LP-filtered rainfall rates based on SPOL, CBM, and TRMM. Lag 0 refers to the
219 time of maximum LP-filtered SPOL rainfall.

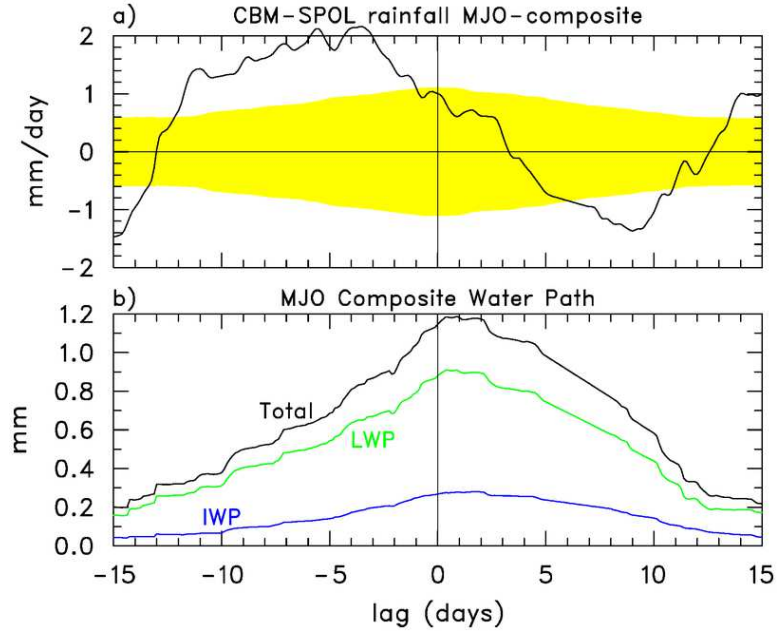
220 Possible explanations for the greater CBM rainfall than observed in the MJO build-up phase
221 include: (1) the storage of cloud and precipitation as the cloud area expands, and (2) the transport
222 of hydrometeors out of the region, say, in the divergent outflow aloft in deep convection. With
223 respect to storage, we first examine the evolution of the area covered by precipitation. It was already
224 shown in Fig. 2 (lower panel) that greater than 50% of the area was covered by high clouds or cirrus
225 around the time of peak MJO rainfall, and from Fig. 3 that the primary contributors to area coverage
226 for echo tops above 5 km were from stratiform precipitation and weak echoes. To examine echo
227 area coverage by lower clouds, Fig. 5 shows a LP-filtered time series of the fraction of the SPOL
228 radar domain occupied by echoes having reflectivity greater than or equal to a -20 dBZ threshold.
229 There is an increase in cloud coverage (or storage) leading up to the MJO rainfall maxima, followed
230 by ~5-10 day periods of peak area coverage (corresponding to stratiform precipitation) succeeded
231 by a rapid falloff. The SPOL time series does not depict the cirrus area coverage since the minimum
232 sensitivity of SPOL is approximately -25 dBZ at 10 km range. In summary, the time series shown
233 in Figs. 2 and 5 provide qualitative evidence of cloud storage.

236 To more quantitatively assess the impact of storage, LWP and IWP data from the Gan CombRet
237 product (Feng et al. 2014) are utilized. Figure 6 compares the difference between CBM and SPOL



234 FIG. 5. Time series of LP-filtered -20 dBZ threshold SPOL echo area coverage. Vertical lines indicate times
 235 of peak LP-filtered SPOL rainfall.

238 composite rainfall (panel a) to the liquid, ice, and total water path in the precipitation systems
 239 at Gan (panel b). The yellow range in the top panel represents an uncertainty estimate for the
 240 CBM-SPOL difference.

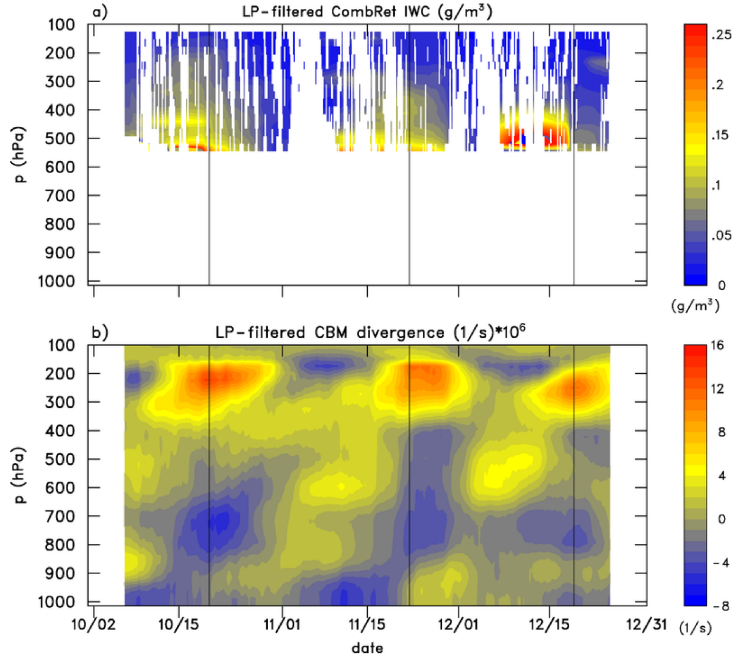


241 FIG. 6. MJO composite of (a) CBM minus SPOL rainfall rate, and (b) CombRet-based LWP, IWP, and total
 242 water path (LWP+IWP). Yellow shading in top panel represents the uncertainty estimate for the CBM-SPOL
 243 rainfall rate difference.

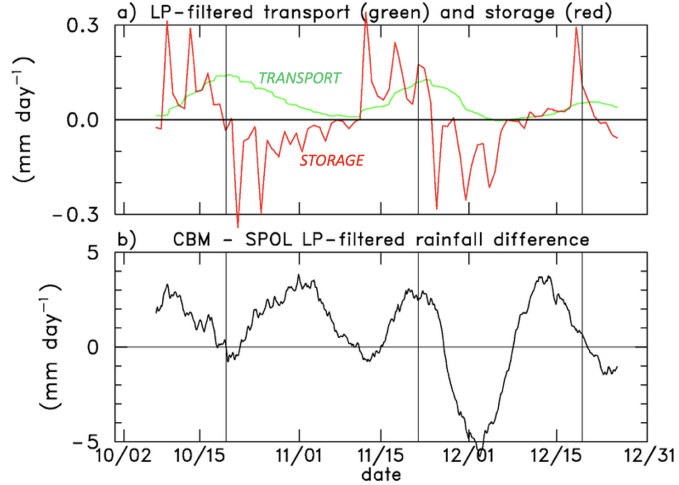
244 It includes (1) a 0.39 mm day^{-1} CBM sampling error (Ciesielski et al. 2021) and (2) SPOL
245 maximum uncertainty estimates as a function of rainfall rate from the DYNAMO Legacy Data
246 Products website (<https://data.eol.ucar.edu/project/DLDP>), both of which are based on 20-day
247 averages. It can be seen that the difference between the CBM and SPOL rainfall rate estimates
248 lies outside the uncertainty range for a ~ 10 -day period in the MJO developing phases and for a
249 ~ 3 -day period in the weakening phase. The increasing total water path leading up to Day 0 and
250 decline afterwards (Fig. 6b) are consistent with the idea that storage and removal, respectively, of
251 hydrometeors can help explain the differences between the diagnosed and observed rainfall rates.
252 While this result is qualitatively consistent with expectations regarding hydrometeor storage, the
253 increase of total water path of $\sim 1 \text{ mm}$ over the 15-day period leading up to Day 0 falls short by at
254 least an order of magnitude in explaining the $1\text{-}2 \text{ mm day}^{-1}$ budget discrepancy (Fig. 6a).

255 Therefore, we next explore the other possible explanation – the transport of hydrometeors out
256 of the region. Satellite imagery of rapidly expanding anvils from individual thunderstorms and
257 mesoscale convective systems suggests that a non-negligible fraction of hydrometeors generated
258 in a storm region may be exported to distant areas where they subsequently precipitate and/or
259 sublimate. This process is often visually dramatic at midlatitudes where strong updrafts are
260 commonplace. Despite weaker updrafts in tropical convection, it may still be important in the
261 tropics. To estimate this effect, the second term on the RHS of (10) is evaluated using ice water
262 content (IWC) data provided by CombRet and divergence fields from the gridded analysis. Here
263 we make the simplifying assumption that IWC is constant over the SPOL averaging area. Also,
264 we only consider ice transport owing to its slow fall speed relative to liquid. Figure 7 shows
265 LP-filtered time series of both the IWC and divergence over the Gan area, the product of which
266 yields an estimate of the transport.

267 Strong peaks in divergence occur in the outflow layer near 200 hPa, where the IWC is quite low
268 ($< 0.1 \text{ g m}^{-3}$). The computed outward transport of hydrometeors integrated over the 150-350 hPa
269 layer is shown in Fig. 8a. Daily-average values can at times be large ($\sim 0.5 \text{ mm day}^{-1}$; not shown),
270 but the LP-filtered transport reaches only $\sim 0.1 \text{ mm day}^{-1}$. This value, as in the case of storage,
271 is at least an order of magnitude below what is needed to explain the CBM-SPOL rainfall rate
272 differences (Fig. 8b). It should be noted, however, that the IWC in the outflow layer may frequently
273 be undersampled due to attenuation by intervening deep convective clouds (Shell et al. 2020).



267 FIG. 7. Time series of LP-filtered (a) CombRet IWC (g m^{-3}) and (b) CBM divergence (10^{-6} s^{-1}) over Gan
268 domain.

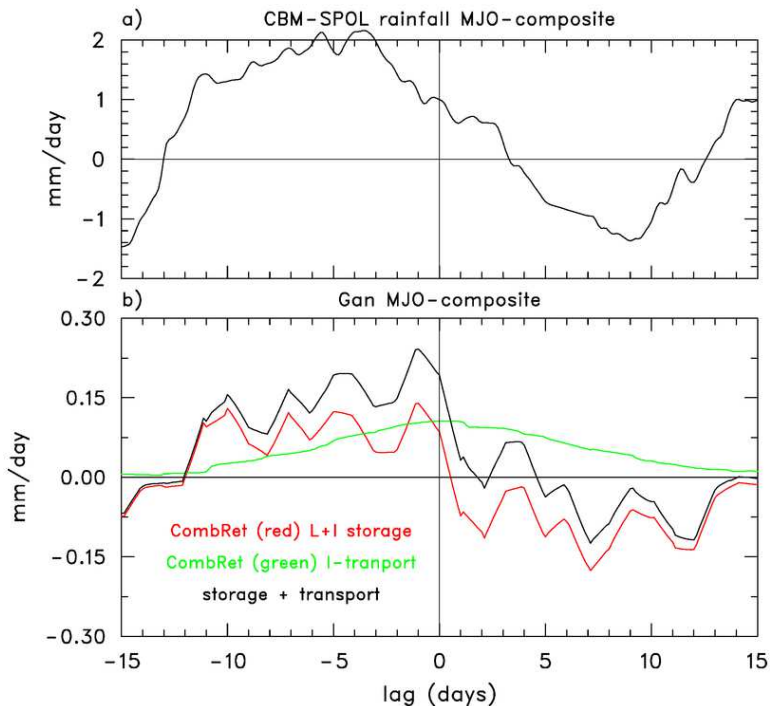


266 FIG. 8. Time series of LP-filtered (a) hydrometeor export (green) integrated over the 15–350 hPa layer and
267 storage (red) and (b) difference in rainfall rate between the conventional budget method and the SPOL radar (mm
268 day^{-1}).

279 Also shown in Fig. 8a is a time series of the storage term. Despite the low-pass filtering, this term
280 is still quite noisy due to high-frequency convective disturbances that move through the region.

281 **4. Discussion**

282 The discrepancy between rainfall rate estimates from sounding-based budgets and radar-based
 283 observations, which is related to storage and transport of hydrometeors, appears to be qualitatively
 284 explained by our analysis of DYNAMO field campaign data. Namely, remote-sensing observations
 285 of hydrometeors on Gan Island combined with sounding data yield estimates of storage and
 286 advection that are in the right direction with respect to expectations. However, comparing Fig. 9a
 287 with Fig. 9b, the estimates fall short by about an order of magnitude in explaining the discrepancies.
 288 The fact that storage and transport are additive in the growing MJO stage and canceling in the
 289 decay stage (Fig. 9b) helps to explain why the magnitude of the CBM-SPOL differences are greater
 290 during the former stage than the latter.



291 FIG. 9. MJO-composite (a) CBM-SPOL rainfall rate difference and (b) estimates of hydrometeor storage (red),
 292 horizontal transport (green), and the sum of the two (black) for SPOL radar domain based on remote sensing and
 293 sounding data.

294 Given that the instrumentation deployed in DYNAMO was probably the best suited to date
 295 to address the storage and transport issue, our expectations were that the calculations from that
 296 campaign would go a long way to explain the budget/radar rainfall rate estimate discrepancies.

297 Since the results fall short of doing so quantitatively, we conclude that even more sophisticated
298 instrumentation, ideally supported by numerical simulations, and improved sounding network
299 designs will be needed in the future to fully address this problem. An example of the limitations
300 with respect to DYNAMO measurements is the underestimation of the IWC of the high-level cirrus
301 (Shell et al. 2020).

302 5. Summary and conclusions

303 Since the pioneering work of Yanai et al. (1973), numerous studies have been carried out to
304 investigate the contributions of convective cloud populations to large-scale heat and moisture
305 budgets using data from atmospheric sounding arrays. The formulations of the conservation
306 equations for heat and moisture used in these studies typically neglect the roles of ice processes
307 as well as the effects of storage and advection of cloud condensate (herein referred to as the
308 conventional budget method or CBM). A more accurate treatment of moist thermodynamics
309 introduced by Ooyama (1990, 2001) has been suggested as being appropriate for studies that have
310 the measurement capabilities to evaluate these typically neglected effects (Schubert et al. 2018).
311 Such measurements were available on Gan Island during the 2011 DYNAMO field campaign and
312 they are used in this paper to estimate hydrometeor storage and advection effects on atmospheric
313 budgets. These measurements include the S-band S-PolKa (SPOL) radar and Ka-band cloud radar
314 (KAZR), both deployed on Gan Island, which were merged by Feng et al. (2014) to produce the
315 combined retrieval product referred to as CombRet.

316 Using the CombRet estimates of ice and liquid water contents and paths, along with the CSU
317 DYNAMO gridded analysis product (Ciesielski et al. 2014), estimates have been made of the
318 storage and advection effects in the thermodynamic budgets. These effects can be interpreted
319 physically in the following way: as the cloud field increases during the developing phase of the
320 MJO, cloud condensate is “stored” in the atmosphere rather than precipitating out immediately.
321 The reverse effect holds true during the decaying phase. In addition, advection in deep convective
322 systems can transport ice hydrometeors into or out of a sampling volume, which can also contribute
323 to errors in traditional budgets that exclude these effects. Equations (8) and (10) contain terms
324 representing these neglected effects.

325 The results of this study, summarized in Fig. 9, show that storage and advective effects deter-
326 mined from measurements obtained from Gan Island along with sounding gridded analyses are
327 qualitatively consistent with the above expectations. Namely, hydrometeor storage and transport
328 effects cause the CBM method to overestimate rainfall rate in the developing stage of the MJO,
329 with the reverse being true during the decaying stage. However, while the findings are qualitatively
330 consistent with expectations, the estimates of their amplitude fall short by an order of magnitude.
331 To better address this issue, future field campaigns would benefit from denser sounding arrays
332 that yield more accurate budgets, sounding arrays that encircle ground-based remote-sensing sys-
333 tems, and improved instrumentation (both ground-based and satellite) that provide more accurate
334 measurements of the content and distribution of hydrometeors in tropical convection.

335 *Acknowledgments.* The authors greatly appreciate the constructive comments and suggestions of
336 three anonymous reviewers. This research has been supported by the National Science Foundation
337 under Grants AGS-1853633 (RHJ) and AGS-1841326 (WHS).

338 *Data availability statement.* The CERES cloud and microphysical data were ob-
339 tained from <http://ceres.larc.nasa.gov/products.php?product=SYN1deg>, the CombRet
340 cloud microphysical data from <https://www.arm.gov/data/pi/71>, the SPOL legacy
341 radar data from <https://data.eol.ucar.edu/project/DLDP>, the TRMM rainfall data from
342 https://disc.gsfc.nasa.gov/datasets/TRMM_3B42_7/summary, the TropFlux surface fluxes
343 from https://incois.gov.in/tropflux/tf_products.jsp, and the CBM gridded diagnosed fields from
344 <https://data.eol.ucar.edu/dataset/347.240>.

345 **References**

- 346 Ciesielski, P. E., L. Hartten, and R. H. Johnson, 1997: Impacts of merging profiler and rawinsonde
347 winds on TOGA COARE analyses. *J. Atmos. Oceanic Technol.*, **14**, 1264–1279.
- 348 Ciesielski, P. E., R. H. Johnson, X. Jiang, Y. Zhang, and S. Xie, 2017: Relationships between
349 radiation, clouds, and convection during DYNAMO. *J. Geophys. Res. Atmos.*, **122**, 2529–2548,
350 <https://doi.org/10.1002/2016JD025965>.

- 351 Ciesielski, P. E., R. H. Johnson, S. Tang, Y. Zhang, and S. Xie, 2021: Comparison of conventional
352 and constrained variational methods for computing large-scale budgets and forcing fields. *J.*
353 *Geophys. Res. Atmospheres*, **126**, <https://doi.org/10.1029/2021JD035183>.
- 354 Ciesielski, P. E., and Coauthors, 2014: Quality controlled upper-air sounding dataset for DY-
355 NAMO/CINDY/AMIE: Development and corrections. *J. Atmos. Oceanic Technol.*, **31**, 741–764,
356 <https://doi.org/10.1175/JTECH-D-13-00165.1>.
- 357 Feng, Z., S. A. McFarlane, C. Schumacher, S. Ellis, J. Comstock, and N. Bharadwaj, 2014:
358 Constructing a merged cloud–precipitation radar dataset for tropical convective clouds during
359 the DYNAMO/AMIE experiment at Addu Atoll. *J. Atmos. Oceanic Technol.*, **31**, 1021–1042,
360 <https://doi.org/10.1175/JTECH-D-13-00132.1>.
- 361 Gallus, W. A., and R. H. Johnson, 1991: Heat and moisture budgets of an intense midlatitude
362 squall line. *J. Atmos. Sci.*, **48** (1), 122–146, [https://doi.org/10.1175/1520-0469\(1991\)048<0122:HAMBOA>2.0.CO;2](https://doi.org/10.1175/1520-0469(1991)048<0122:HAMBOA>2.0.CO;2).
- 363
- 364 Gottschalck, J., P. E. Roundy, C. J. S. III, A. Vintzileos, and C. Zhang, 2013: Large-scale
365 atmospheric and oceanic conditions during the 2011-12 DYNAMO field campaign. *Mon. Wea.*
366 *Rev.*, **141**, 4173–4196, <https://doi.org/10.1175/MWR-D-13-00022.1>.
- 367 Hamming, R. W., 1989: *Digital filters*. Dover, 284 pp.
- 368 Huffman, G. J., R. F. Adler, D. T. Bolvin, G. Gu, E. J. Nelkin, K. P. Bowman, E. F. Stocker, and
369 D. B. Wolff, 2007: The TRMM multi-satellite precipitation analysis: Quasi-global, multi-year,
370 combined-sensor precipitation estimates at fine scale. *J. Hydrometeor.*, **8**, 33–55, <https://doi.org/10.1175/JHM560.1>.
- 371
- 372 Johnson, R. H., 1980: Diagnosis of convective and mesoscale motions during phase III of GATE.
373 *J. Atmos. Sci.*, **37**, 733–753, [https://doi.org/10.1175/1520-0469\(1980\)037<0733:DOCAMM>2.0.CO;2](https://doi.org/10.1175/1520-0469(1980)037<0733:DOCAMM>2.0.CO;2).
- 374
- 375 Johnson, R. H., and P. E. Ciesielski, 2000: Rainfall and radiative heating rate estimates from
376 TOGA COARE atmospheric budgets. *J. Atmos. Sci.*, **57**, 1497–1514, [https://doi.org/10.1175/1520-0469\(2000\)057<1497:RARHRF>2.0.CO;2](https://doi.org/10.1175/1520-0469(2000)057<1497:RARHRF>2.0.CO;2).
- 377

- 378 Johnson, R. H., P. E. Ciesielski, J. H. R. Jr., and M. Katsumata, 2015: Sounding-based
379 thermodynamic budgets for DYNAMO. *J. Atmos. Sci.*, **72** (2), 598–622, <https://doi.org/10.1175/JAS-D-14-0202.1>.
- 380
- 381 Madden, R. A., and P. R. Julian, 1971: Detection of a 40–50 day oscillation in the zonal wind in the
382 tropical Pacific. *J. Atmos. Sci.*, **28**, 702–708, [https://doi.org/10.1175/1520-0469\(1971\)028<0702:DOADOI>2.0.CO;2](https://doi.org/10.1175/1520-0469(1971)028<0702:DOADOI>2.0.CO;2).
- 383
- 384 Mapes, B. E., P. E. Ciesieslki, and R. H. Johnson, 2003: Sampling errors in rawinsonde-array
385 budgets. *J. Atmos. Sci.*, **60**, 2697–2714.
- 386
- 387 McNab, A. J., and A. K. Betts, 1978: A mesoscale budget study of cumulus convection. *Mon. Wea. Rev.*, **106** (9), 1317–1331, [https://doi.org/10.1175/1520-0493\(1978\)106<1317:AMBSOC>2.0.CO;2](https://doi.org/10.1175/1520-0493(1978)106<1317:AMBSOC>2.0.CO;2).
- 388
- 389 Moum, J. N., and Coauthors, 2014: Air-sea interactions from westerly wind bursts during the
390 November 2011 MJO in the Indian Ocean. *Bull. Amer. Meteor. Soc.*, **95** (8), 1185–1199,
391 <https://doi.org/10.1175/BAMS-D-12-00225.1>.
- 392
- 393 Ooyama, K. V., 1990: A thermodynamic foundation for modeling the moist atmosphere. *J. Atmos. Sci.*, **47**, 2580–2593, [https://doi.org/10.1175/1520-0469\(1990\)047<2580:ATFFMT>2.0.CO;2](https://doi.org/10.1175/1520-0469(1990)047<2580:ATFFMT>2.0.CO;2).
- 394
- 395 Ooyama, K. V., 2001: A dynamic and thermodynamic foundation for modeling the moist at-
396 mosphere with parameterized microphysics. *J. Atmos. Sci.*, **58**, 2073–2102, [https://doi.org/10.1175/1520-0469\(2001\)058<2073:ADATFF>2.0.CO;2](https://doi.org/10.1175/1520-0469(2001)058<2073:ADATFF>2.0.CO;2).
- 396
- 397 Peixoto, J. P., and A. H. Oort, 1992: *Physics of Climate*. American Institute of Physics, 520 pp.
- 398
- 399 Powell, S. W., R. A. Houze, Jr., and S. R. Brodzik, 2016: Rainfall-type categorization of radar
400 echoes using polar coordinate reflectivity. *J. Atmos. Sci.*, **33**, 523–538, <https://doi.org/10.1175/JTECH-D-15-0135.1>.
- 401
- 402 Praveen Kumar, B., J. Vialard, M. Lengaigne, V. S. N. Murty, M. J. McPhaden, M. F. Cronin,
403 F. Pinsard, and K. Gopala Reddy, 2012: TropFlux wind stresses over the tropical oceans: eval-
404 uation and comparison with other products. *Climate Dynamics*, **40**, 2049–2071, <https://doi.org/10.1007/s00382-012-1455-4>.

- 405 Schubert, W. H., P. E. Ciesielski, and R. H. Johnson, 2018: Heat and moisture budget analysis with
406 an improved form of moist thermodynamics. Cornell University, arXiv: 1810.11119 [physics.ao-
407 ph], 14 pp.
- 408 Shell, K. M., S. P. de Szeke, M. Makiyama, and Z. Feng, 2020: Vertical structure of the
409 radiative heating rates of the MJO during DYNAMO. *J. Climate*, **33**, 5317–5335, <https://doi.org/10.1175/JCLI-D-19-0519.1>.
- 410
- 411 Virts, K. S., and R. A. Houze, Jr., 2015: Clouds and water vapor in the tropical tropopause
412 transition layer over mesoscale convective systems. *J. Atmos. Sci.*, **72**, 4739–4753, <https://doi.org/10.1175/JAS-D-15-0122.1>.
- 413
- 414 Wielicki, B. A., B. R. Barkstrom, E. F. Harrison, R. B. Lee, G. L. Smith, and J. E. Cooper, 1996:
415 Clouds and the Earth's Radiant Energy System (CERES): An earth observing system experiment.
416 *Bull. Amer. Meteor. Soc.*, **77** (5), 853–868, [https://doi.org/10.1175/1520-0477\(1996\)077<0853:CATERE>2.0.CO;2](https://doi.org/10.1175/1520-0477(1996)077<0853:CATERE>2.0.CO;2).
- 417
- 418 Xu, W., and S. A. Rutledge, 2014: Convective characteristics of the Madden-Julian Oscillation
419 over the central Indian Ocean observed by shipborne radar during DYNAMO. *J. Atmos. Sci.*,
420 **71** (8), 2859–2877, <https://doi.org/10.1175/JAS-D-13-0372.1>.
- 421
- 422 Xu, W., S. A. Rutledge, C. Schumacher, and M. Katsumata, 2015: Evolution, properties and spatial
423 variability of MJO convection near and off the equator during DYNAMO. *J. Atmos. Sci.*, **72**,
424 4126–4147, <https://doi.org/10.1175/JAS-D-15-0032.1>.
- 425
- 426 Yanai, M., S. Esbensen, and J.-H. Chu, 1973: Determination of bulk properties of tropical cloud
427 clusters from large-scale heat and moisture budgets. *J. Atmos. Sci.*, **30**, 611–627, [https://doi.org/10.1175/1520-0469\(1973\)030<0611:DOBPOT>2.0.CO;2](https://doi.org/10.1175/1520-0469(1973)030<0611:DOBPOT>2.0.CO;2).
- 428
- 429 Yanai, M., and R. H. Johnson, 1993: Impacts of cumulus convection on thermodynamic fields.
430 *Meteor. Monogr.*, **24**, 39–62, <https://doi.org/10.1175/0065-9401-24.46.1>.
- 431
- 432 Yoneyama, K., C. Zhang, and C. N. Long, 2013: Tracking pulses of the Madden-Julian Oscillation.
433 *Bull. Amer. Meteor. Soc.*, **94**, 1871–1891, <https://doi.org/10.1175/BAMS-D-12-00157.1>.
- 434

- 431 Yu, H., R. H. Johnson, P. E. Ciesielski, and H.-C. Kuo, 2018: Observation of quasi-2-day convective
432 disturbances in the equatorial Indian Ocean during DYNAMO. *J. Atmos. Sci.*, **75**, 2867–2888,
433 <https://doi.org/10.1175/JAS-D-17-0351.1>.
- 434 Zuluaga, M. D., and R. A. Houze, Jr., 2013: Evolution of the population of precipitating convective
435 systems over the equatorial Indian Ocean in active phases of the Madden–Julian Oscillation. *J.*
436 *Atmos. Sci.*, **70**, 2713–2725, <https://doi.org/10.1175/JAS-D-12-0311.1>.